Journal of Materials Chemistry A

Synergistic enhancement of chemical looping CO2 splitting and biomass cascade utilization using cyclic stabilized Ca2Fe2O5 aerogel

Journal:	*Journal of Materials Chemistry A*
Manuscript ID	TA-ART-10-2018-010277.R1
Article Type:	Paper
Date Submitted by the Author:	11-Dec-2018
Complete List of Authors:	Sun, Zhao; Southeast University; University of Wyoming, Chemical Engineering Wu, Xiaodong; Nanjing Tech University, College of Materials Science and Enginering Nanjing, China Russell, Christopher; Stanford University, Civil & Environmental Engineering; Purdue University, Chemical Engineering Dyar, M. D.; Mt Holyoke Coll Sklute, Elizabeth; Mount Holyoke College, Department of Astronomy; Planetary Science Institute, Toan, Sam; University of Wyoming, Department of Chemical and Petroleum Engineering Fan, Maohong; University of Wyoming, Department of Chemical and Petroleum Engineering Duan, Lunbo; Southeast University, Xiang, Wenguo; Southeast University, School of Energy and Environment

Journal of Materials Chemistry A

PAPER

Synergistic enhancement of chemical looping-based CO_2 splitting with biomass cascade utilization using cyclic stabilized $Ca_2Fe_2O_5$ aerogel

Received 00th January 20xx,
Accepted 00th January 20xx

DOI: 10.1039/x0xx00000x

www.rsc.org/

Zhao Sun [ab], Xiaodong Wu [b], Christopher K. Russell [c], M. Darby Dyar [d], Elizabeth C. Sklute [d], Sam Toan [b], Maohong Fan *[b], Lunbo Duan [a], Wenguo Xiang *[a]

Thermochemical splitting of carbon dioxide to carbon-containing fuels or value-added chemicals is a promising method to reduce greenhouse effects. In this study, we propose a novel process for synchronous promotion of chemical looping-based CO_2 splitting with biomass cascade utilization. The superiority of the process is reflected in 1) A biomass fast pyrolysis process is carried out for syngas, phenolic-rich bio-oil, biochar co-production with oxygen carrier reduction; 2) the reduced oxygen carrier and the biomass-derived biochar were both applied for CO_2 splitting during the oxygen carrier oxidation stage with carbon monoxide production as well as oxygen carrier re-oxidation; 3) the redox looping of the oxygen carrier was found to synchronously promote the comprehensive utilization of biomass and CO_2 splitting to CO. Various characterizations e.g. HRTEM- and SEM-EDX mapping, H_2-TPR, CO_2-TPO, XRD, XPS, N_2 nitrogen adsorption and desorption isotherms test, Mössbauer, etc. were employed to elucidate the aerogels' microstructures, phase compositions, redox activity, and cyclic stability. Results indicate that the $Ca_2Fe_2O_5$ aerogel is a promising initiator of the proposed chemical looping process from the perspectives of biomass utilization efficiency, redox activity, and cyclic durability.

1. Introduction

Emission of carbon dioxide (CO_2) in the atmosphere has been shown to be a significant cause of global climate change [1, 2]. The atmospheric CO_2 concentration has risen to >400 ppm since the industrial revolution and is projected to continue to rise if anthropogenic sources remain unchecked [3]. Currently, carbon capture and storage (CCS) is considered the primary mechanism for reducing CO_2 emissions [4-6]. However, this emission reduction may be inadequate compared to the projected increase in anthropogenic CO_2 emissions[7].

One potentially sustainable way to mitigate carbon emissions is to utilize CO_2 to generate value-added chemicals or fuels [8-11]. Five main approaches have been explored for CO_2 conversion and utilization (CCU): photosynthetic conversion, electrochemical reduction, CO_2 fixation [12, 13], solar thermochemical splitting [14-17], and chemical looping splitting. Mallapragada et al. performed a Sun-to-Fuel assessment indicating that the CO_2 fixing efficiency of biological processes (i.e. photosynthesis) is relatively low [18]. Electrochemical conversion of carbon dioxide offers a promising approach to mitigate anthropogenic CO_2 emissions, however, the rapid degradation of the electrode materials, including carbon deposition-induced cathode/electrolyte delamination, remains a significant challenge, making durable catalysts capable of converting CO_2 to CO highly desirable [19-21]. Carbon fixation using porous coordination polymers (PCPs) or microporous organic networks (MONs) is novel, but the CO_2 conversion efficiency and catalytic cost need further investigation. Thermochemical splitting requires high operating temperatures, leading to expensive reactor design and materials, and requires quenching to prevent re-oxidation of the products, leading to an energy penalty of up to 80% of the solar input [23]. Thus, the commercial application of solar splitting of CO_2 or H_2O technology still faces several major challenges.

Catalyst-assisted chemical looping-based CO_2 splitting is an emerging technology where a solid, named as an oxygen carrier (OC), transports oxygen via cyclic reduction and oxidation [19-22]. During the reduction stage, a gas reduces the OC with the production of CO_2 and/or H_2O, and the reduced OC is then used to reduce CO_2 to CO. The process is known as chemical looping methane reforming (CLMR)[23-27] or reverse water-gas shift chemical looping (RWGS-CL)[28, 29] when CH_4 or H_2 is the reducing agent, respectively. The presence of the reducing gas reduces the required temperature for CO_2 splitting. The selection of a high-performance oxygen carrier capable of being reduced and oxidized over multiple redox cycles without significant deactivation is a key consideration for the development of

[a] Key Laboratory of Energy Thermal Conversion and Control of Ministry of Education, School of Energy and Environment, Southeast University, Nanjing 210096, China. *Email: wgxiang@seu.edu.cn; lunboduan@seu.edu.cn.
[b] Departments of Chemical and Petroleum Engineering, University of Wyoming, Laramie, WY 82071, USA *Email: mfan@uwyo.edu
[c] Department of Civil and Environmental Engineering, Stanford University, Stanford, CA 94305, USA
[d] Mount Holyoke College, Department of Earth & Environment, South Hadley, MA 01075, USA
[e] Center for Advanced Materials Characterization, University of Oregon, Eugene, OR 97403, USA

chemical looping CO_2 splitting processes. Iron oxide is promising due to its abundance, innocuity, and reduced toxicity compared with Cu, Ni, Mn, and Co [30-32]. However, when pure iron oxide is used as an oxygen carrier, deactivation occurs in the first few cycles [19, 20]. To resist sintering and agglomeration, materials such as Al_2O_3, CeO_2, MgO, $MgAl_2O_4$, ZrO_2, and SiO_2 are alloyed with the iron oxide [33-39]. However, degradation of oxygen carriers remains inevitable, and the generated spinel will decrease the oxygen storage capacity of the synthesized iron oxides [40, 41]. Additionally, because CO_2 is a weaker reducing agent than O_2, Fe-based oxygen carriers generally cannot be completely oxidized to Fe^{3+}, resulting in the production of Fe_3O_4 ($Fe^{3+,\ 2+}$) rather than Fe_2O_3 (Fe^{3+}). Comparatively, the reduced $Ca_2Fe_2O_5$ (mixture of CaO and Fe^0) can be completely oxidized by H_2O or CO_2 and re-generate Fe^{3+} in one step [42, 43]. The overall reactions for the CO_2 splitting process by using Fe_2O_3 and $Ca_2Fe_2O_5$ are shown as follows:

$$3Fe + 4CO_2 \rightarrow Fe_3O_4 + 4CO \quad \text{(R1)}$$

$$3CO_2 + 2Fe + 2CaO \rightarrow Ca_2Fe_2O_5 + 3CO \quad \text{(R2)}$$

Comparing (R1) and (R2) indicates that the utilization efficiency of Fe valence between Fe_2O_3 and $Ca_2Fe_2O_5$ is different. Without the presence of Ca, the reduced OC (Fe^0) could only be oxidized by CO_2 to generate Fe_3O_4, instead of Fe_2O_3, yielding 1.33 mol·CO/mol·Fe, whereas 1.50 mol·CO/mol·Fe can be produced for $Ca_2Fe_2O_5$. Thus, with the same moles of Fe oxidization by CO_2, the CO production by using $Ca_2Fe_2O_5$ is expected to increase by 12.5%.

To minimize the CO_2 splitting temperature and improve the cyclic stability of the OC, aerogel materials can be implemented. Aerogels are porous materials composed of polymers or nanoparticles with low density, large BET surface area, low thermal conductivity, and high thermal stability [44]. The material properties make them broadly applicable, including in catalysis, energy adsorption and storage, and chemical sensing [45, 46]. Typically, metal oxide aerogels can be formed by hydrolyzing and condensing metal alkoxide precursors [47, 48]. However, this method is not suitable for the preparation of low valence metal oxide gels such as NiO, CuO, CaO, and ZnO [49-51]. Instead, a dispersed inorganic sol-gel (DIS) method using propylene oxide (PO) and polyacrylic acid (PAA) is necessary. [20, 52-54].

Remarkably, few studies have reported the preparation and application of Ca-Fe composite aerogels as the OC for the simultaneous enhancement of chemical looping CO_2 splitting and biomass cascade utilization. In this study, Ca-Fe composite aerogels, $Ca_2Fe_2O_5$ and $CaFe_2O_4$, were designed *via* a freeze-dry-assisted DIS method. The prepared aerogel materials were then used as the OCs for chemical looping [52]. We propose a process that combines biomass fast pyrolysis and biochar gasification with chemical looping combustion (CLC) for the synergistic promotion of biomass cascade utilization and CO_2 splitting to CO using the designed oxygen carrier. The schematic illustration of the chemical looping process is presented in Fig. 1. The evolution of microstructures, phase compositions, redox activity, cyclic stability, and promotion mechanisms were investigated.

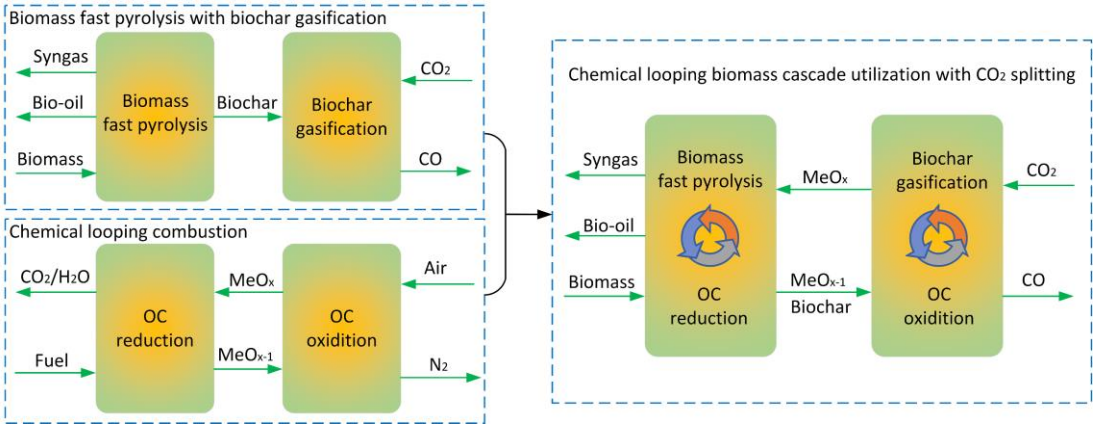

Fig. 1 Schematic illustration of chemical looping biomass cascade utilization combined with CO_2 splitting process.

2. Experimental

2.1 Material preparation

$Ca(NO_3)_2{\cdot}4H_2O$ (Sigma-Aldrich C1396-500G), $Fe(NO_3)_3{\cdot}9H_2O$ (Sigma-Aldrich 216828-500G), poly-acrylic acid (Sigma-Aldrich 323667-100G), and propylene oxide (C_3H_6O, Sigma-Aldrich 110205-500ML) were used as raw materials. All the reagents and solvents were analytical grade and used as received without further purification. In a typical synthesis, 0.01 mol $Ca(NO_3)_2{\cdot}4H_2O$ and 0.01 mol $Fe(NO_3)_3{\cdot}9H_2O$ were dissolved in a mixture of 10 mL DI water and 10 mL ethanol, which was then stirred for 30 min at room temperature. Next, 1.0 g poly-acrylic acid (PAA) and 2 mL propylene oxide (PO) (C_3H_6O, Sigma-Aldrich 110205-500ML) were added, stirring between each addition. The mixture was then transferred to a plastic mold for further gelation and aged for 48 h at room temperature before being frozen for 15 min using liquid nitrogen. The frozen sample was then vacuum dried at room temperature to induce ice sublimation. The generated Ca/Fe composite aerogel was subsequently calcined at a heat rate of 3 °C/min from 25 to 850 °C with a dwell time of 3 h. The resulting aerogel was ground into a fine powder with an agate mortar and pestle (See Fig. S1 for the aerogel preparation details).

2.2 Material characterization

Crystallinity and chemical components of fresh, syngas

reduced, and cycled aerogel samples (oxygen carriers) were determined using a Rigaku Smartlab X-ray diffractometer (XRD) (40 kV, 40 mA using a Cu Kα radiation source). The XRD patterns were collected in the 2θ range from 20 to 80° with a step of 0.02° and 15 s counting time per angle. The Brunauer-Emmett-Teller (BET) surface areas of the materials were determined by N_2 adsorption at -196 °C (after 6 h outgassing at 150°C). Raman spectra are collected on an Advantage 785 Raman Spectrometer (785 nm wavelength, 100 mW peak power). The chemical state of the OC was determined using X-ray photoelectron spectroscopy (XPS) (Thermo-scientific ESCALAB 250, Al Kα monochromatic X-ray source, 500 µm spot size, 150 eV survey scans, 20 eV composition scans) with a low-energy electron flood for charge neutralization.

Surface morphology characterization and microstructure observation of fresh and reacted aerogels was conducted using SEM (FEI Quanta FEG 450) and TEM (FEI Technai C2 F20 S-Twin, 300 kV with 1 nA beam current), and Ca and Fe element distribution was examined using energy dispersive spectrometry (EDS). Temperature-programmed reduction (TPR) measurement was carried out in a Quantachrome TPx automated gas sorption analyzer. For each characterization, 0.10 g of sample was loaded in a quartz reactor and out-gassed by helium at 150 °C for 30 min. The sample was then cooled to 30 °C and 5% H_2 in N_2 was flowed over the surface for 60 min. The temperature was ramped from 30 to 1050 °C (5 °C/min heat rate). CO_2-temperature programmed oxidation (CO_2-TPO) was performed in an SDT Q600 thermo gravimetric analyzer (30 mg sample, 10°C/min heat rate, 25 to 1000°C, N_2 and CO_2 flow rates 45 and 5 mL/min, respectively).

Mössbauer sample mounts were prepared by grinding 30 mg aerogel and sugar in a diamonite mortar and pestle and storing in plastic washers confined with Kapton tape. Mössbauer measurements were taken at 295K, on a Web Research Co. (now See Co.) W100 spectrometer using a ~100-80 mCi ^{57}Co source in rhodium (12-24 hr run time). Spectra were collected in 1024 channels and 122 keV gamma ray Compton scattering corrections were applied by electrons inside the detector. The corrected data are equal to A/(1-b), where A is the counts of the uncorrected absorption and b is the Compton fraction determined through recording the counts with and without a 14.4 keV stop filter (~ 2 mm Al foil) in the gamma ray beam. Notably, this correction does not change the results of the fits, it does allow for accurate determination of the percent absorption in each spectrum. Each spectrum was then folded and corrected for nonlinearity in WMOSS, a Mössbauer spectra analysis software. Interpolation to a linear-velocity scale was performed using a 25 µm α-Fe foil standard at room temperature. Samples were fit using Mex_disd, which solves the full hyperfine interaction Hamiltonian for multiple distributions and minimizes the chi squared deviation between the fitted and experimental spectrum using center shift, quadrupole shift, full width at half maximum, and distribution area as free parameters, but allows for a distribution of hyperfine fields within a specified range [55].

Pine wood fast pyrolysis product identification was performed using gas chromatography/mass spectrometry (Agilent 7890B/5977B with G4513A ALS autoinjector, 250°C inlet temperature, 10: 1 split ratio, 1.0 mL/min He carrier flow rate). The products were separated by a HP-5 MS Ultra Inert capillary column (30 m × 0.25 mm × 0.25 µm). The GC column was held at 40 °C for 3 min followed by heating from 40 to 300 °C at 3 °C /min and held at 300 °C for 10 min. The temperatures in the interface, electron-ion source (EI), and quadrupole analyzer are set to be 250 °C, 230 °C, and 150 °C, respectively. The EI source was operated in the electron impact mode with 70 eV electrons, and fragmental ion EI products were separated by the quadrupole analyzer and ions m/z ranging from 33 to 550 were scanned by an electron multiplier. Product identification was performed based on the NIST database of MS spectra. Peak area (%) and relative component content determined by area normalization was used to estimate the detected bio-oil compositions.

2.3 Reaction setup and procedures

$Ca_2Fe_2O_5$ and $CaFe_2O_4$ catalytic activity and cyclic stability were investigated using thermogravimetric analysis (TGA) or a vertical fixed bed reactor. The effect of varied materials (Fe_2O_3, $Ca_2Fe_2O_5$, and $CaFe_2O_4$), reducing agents (CH_4, CO, H_2, and CH_4 + CO + H_2), reduction temperatures (700 °C, 750 °C, 800 °C, 850 °C, and 900 °C), and CO_2 oxidation temperatures (700 °C, 750 °C, 800 °C, 850 °C, and 900 °C) were investigated via TGA. In a typical experiment, around 10 mg sample was heated from room temperature to a specified reduction temperature before reducing agent/agents were flowed over the surface of the sample for 40 min, followed by 20 min CO_2 oxidation.

Biomass fast pyrolysis (OC reduction) and CO_2 splitting (OC oxidation) experiments were conducted using a fixed bed reactor (See Fig. S1). In a typical experiment, 2.000 ± 0.0020 g of beetle eroded pine wood (powder, particle size less than 0.25 µm, Table 1 and Table 2) and 0.2000 ± 0.0002 g of oxygen carrier (Fe_2O_3, $Ca_2Fe_2O_5$, or $CaFe_2O_4$) were ground using an agate mortar until well mixed. The mixture was then loaded into the constant temperature area of the quartz tube reactor (i.d. 10 mm) and purged with 60 mL/min N_2. Biomass fast pyrolysis was initiated after the furnace stabilized at the oxidation temperature, and maintained for 40 min. CO_2 splitting began when the diluent was changed from N_2 (60 mL/min) to N_2/CO_2 (120 mL/min, 1: 1 vol. ratio) and was maintained for 180 min.

Cyclic stability tests were carried out at 800 °C using both TGA and a fixed bed reactor for fifty continuous redox cycles. To compare the cumulative CO production, same mole (0.0025 mol) of oxygen carrier were added for each fixed bed experiments. Biomass-derived syngas was substituted with a gas mixture (14.22 vol.% H_2, 8.66 vol.% CH_4, 21.93 vol.% CO, and 55.19 vol.% N_2, 60 mL/min N_2) for chemical looping-based CO_2 splitting experiments. A 44.81 vol. % CO_2 in N_2 (60 mL/min) is used for CO production, with 30 min OC reduction and 10 min CO_2 splitting cycles split by 10 min N_2 purges. All products (H_2, CH_4, CO, and CO_2) were analyzed by INFICON micro gas chromatography (GC) 3000.

3 Results and discussion

3.1 As-prepared OC characterization

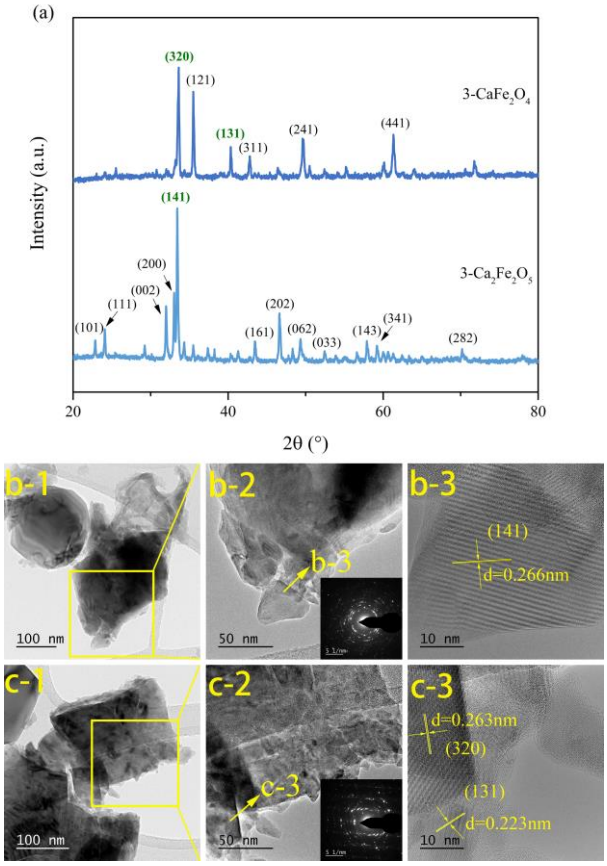

Fig. 2. a) XRD patterns of $Ca_2Fe_2O_5$ and $CaFe_2O_4$ aerogels; b) TEM images of $Ca_2Fe_2O_5$ aerogel; c) TEM images of $CaFe_2O_4$ aerogel.

The X-ray diffraction (XRD) results indicate the presence of $Ca_2Fe_2O_5$ (JCPDS: 71-2264) and $CaFe_2O_4$ (JCPDS: 72-1199) for aerogels prepared with 1 and 2 Ca: Fe mol ratios, respectively (Fig. 2a). The $Ca_2Fe_2O_5$ aerogel XRD pattern has peaks at 31.9°, 33.0°, 33.4°, and 46.6°, corresponding to (002), (200), (141), and (202) facets. The peaks of fresh $CaFe_2O_4$ aerogel are located at 33.6° (320), 35.4° (121), 40.3° (131), 49.5° (241), and 61.2° (441). The lattice morphology of the samples is observed clearly according to the HRTEM images (See Fig. 2c-3). The particles with a d spacing of 0.266 nm were related to the (141) $Ca_2Fe_2O_5$ facet and the particles with the d spacing of 0.263 nm and 0.223 nm were associated with the (320) and (131) facet, respectively.

The near surface region of as-prepared $Ca_2Fe_2O_5$ and $CaFe_2O_4$ is analyzed by X-ray photoelectron spectroscopy (XPS) to determine the elemental distributions as seen in Fig. 3. The full-range XPS spectra confirms the presence of the intended aerogels with atomic concentrations of 6.2% Fe, 54.6% O, 17.1% Ca, and 22.1% C for $Ca_2Fe_2O_5$ and 8.2% Fe, 41.9% O, 8.7% Ca, and 41.3% C for $CaFe_2O_4$ (Fig. 3a). High-resolution XPS spectra of Ca_{2p}, Fe_{2p}, and C_{1s} were analyzed to determine the chemical environment and the surface compositions of the $Ca_2Fe_2O_5$/$CaFe_2O_4$ as displayed in Fig. 3b. The observed binding energies of $Ca2p_{½}$ at 350.3 eV and $Ca2p_{3/2}$ at 346.8 eV corresponds to $CaCO_3$ [56]. Take $Ca_2Fe_2O_5$ for analysis, the two Ca peaks for $2p_{3/2}$ at 345.7 eV and $2p_{1/2}$ at 349.1 eV together with a Fe $2p_{3/2}$ peak at 709.6 eV and $2p_{1/2}$ peak at 722.9 eV corresponds to $Ca_2Fe_2O_5$ [20]. It is also concluded that the Ca2p peak moves to higher binding energy (345.6 eV→345.7 eV→346.3eV) and Fe2p peak shifts to lower binding energy (710.7 eV→710.4 eV→709.6 eV) with the increase of Ca/Fe mole ratio, indicating the electron transformation from Ca to Fe. A certain portion of the C_{1s} peaks at 289.3 eV and 284.9 eV is associated with $CaCO_3$ and C, respectively, indicating that calcium carbonate and carbon are formed on the surface of the aerogels during preparation.

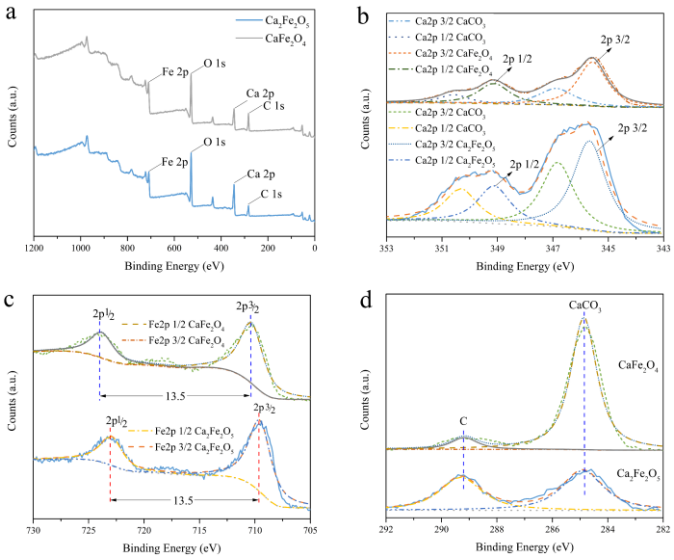

Fig. 3. Large scale (a) and high resolution XPS spectra of $Ca_2Fe_2O_5$ and $CaFe_2O_4$ aerogels for Ca_{2p} (b), Fe_{2p} (c), and C_{1s} (d) peaks.

3.2 Redox activity and cyclic stability tests

The effects of different oxygen carriers, reducing agents, as well as reduction and oxidation temperatures on the activity of OC reduction and CO_2 splitting are investigated using TGA. (See Fig. 4). To mimic pine wood fast pyrolysis, a mixture of 14.29 vol.% H_2, 8.69 vol.% CH_4, and 22.02 vol.% CO in N_2 was used for OC reduction at 800 °C. As can be seen from Fig. 4a, the syngas reduction activity at 800 °C trends inversely with the Ca content, specifically Fe_2O_3 > $CaFe_2O_4$ > $Ca_2Fe_2O_5$. This is because the lattice oxygen in Fe_2O_3 is more active than that of $CaFe_2O_4$ and $Ca_2Fe_2O_5$ at a relatively low temperature. It is also observed that once the $Ca_2Fe_2O_5$ or $CaFe_2O_4$ (Fe^{3+}) is near completely reduced by the syngas, carbon is more inclined to be deposited on the surface of $Ca_2Fe_2O_5$ and $CaFe_2O_4$ samples. More importantly, carbon deposited on the reduced $Ca_2Fe_2O_5$ or $CaFe_2O_4$ samples enabled oxidization by CO_2 and regeneration of Fe^{3+} in a single step with CO_2 splitting to CO. In this case, the deposited carbon during the reduction step increases CO production.

Reducing agents, in order of reduction activity for $Ca_2Fe_2O_5$ is H_2 > CO > syngas > CH_4 (Fig. 4b). Carbon deposition starts when $Ca_2Fe_2O_5$ aerogel approaches complete reduction when CO or syngas are the reducing agent. The carbon was deposited even earlier when CH_4 is used due to the fast deposition of carbon. Larger quantities of carbon tend to be deposited on the reduced OC when syngas is used as the reducing agent compared to CO and CH_4 which could be attributed to both CH_4 decomposition and CO disproportionation.

Unsurprisingly, syngas reduction rate increases with increasing reduction temperature as can be seen from Fig. 4c. While carbon production tends to increase linearly with time at 800 °C, carbon deposition increases until 800 °C and then decreases gradually. As seen in Fig.4d, there are no obvious mass decreasing at 700 °C, indicating the inadequate temperature for deposited carbon gasification during CO_2 splitting. The deposited carbon can be partially oxidized by CO_2 at 750 °C, but the gasification rate is rather slow. Thus, the weight increase at the low temperature range is concluded to be the comprehensive reactions of OC oxidation, CaO carbonation, and low reaction rate carbon gasification. At temperatures above 800 °C, the CO_2 splitting stage can be divided into three stages: 1) Deposited carbon removal with CO_2 splitting, resulting in the mass decrease; 2) Fe^0 oxidization by CO_2 to generate $Ca_2Fe_2O_5$; 3) complete oxidization of OC, leading to the mass stable. Thus, 800 °C is the minimum recommended temperature and a desirable choice for OC re-generation.

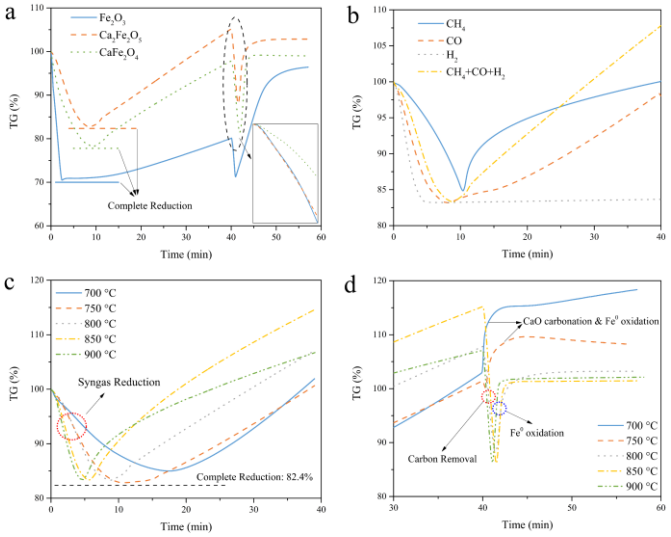

Fig. 4. OC reduction residue (%) as a function of reaction time in the presence of different (a) OCs, (b) reduction agents over $Ca_2Fe_2O_5$ at 800 °C, (c) reduction temperatures on $Ca_2Fe_2O_5$, and (d) oxidation temperatures on reduced $Ca_2Fe_2O_5$.

The fixed bed reactor experiments include two stages: chemical looping biomass cascade utilization and CO_2 splitting. For the first stage, syngas, phenolic-rich bio-oil, and biochar were produced during fast pyrolysis of pine wood with OC reduction. Here, the OC supplies lattice oxygen for bio-tar cracking, generating CO_2, H_2O, and CaO. The presence of CaO was reported to promote tar cracking, thereby promoting heavy oil to light oil transformation, subsequently increasing gaseous and liquid products [54, 57-59]. During CO_2 splitting, the reduced OC is re-oxidized by CO_2 to re-generate $Ca_2Fe_2O_5$ and CO_2 is reduced to CO. Additionally, deposited carbon can be oxidized by CO_2 with CO production. Introduction of Fe_2O_3, $Ca_2Fe_2O_5$, or $CaFe_2O_4$ increased the liquid production by 13.8%, 10.7%, and 16.5%, respectively, comparing biomass fast pyrolysis without OC addition (See Fig. 5a and Fig. S2). Remarkably, the maximum yield of biochar is obtained using $Ca_2Fe_2O_5$, which could also be used for CO_2 splitting.

The bio-oil produced from pine wood fast pyrolysis is investigated by GCMS and the bio-oil component is analyzed using the detected peak areas (See Fig. 5b). The bio-oils produced during pine wood fast pyrolysis were classified to be aromatic compounds, heterocyclic compounds, alicyclic compounds, and chain compounds (See SI). The aromatic compounds' concentration increased compared to non-catalytic biomass pyrolysis, especially in the presence of $Ca_2Fe_2O_5$. The percentage of chain compounds also decreased with the addition of OC, suggesting that the lattice oxygen is beneficial for chain compound conversion. The percentage of phenolic compounds accounts for 45.9%, 42.4%, 45.6%, and 46.0% of pyrolysis products in the presence of Fe_2O_3, $Ca_2Fe_2O_5$, and $CaFe_2O_4$, respectively.

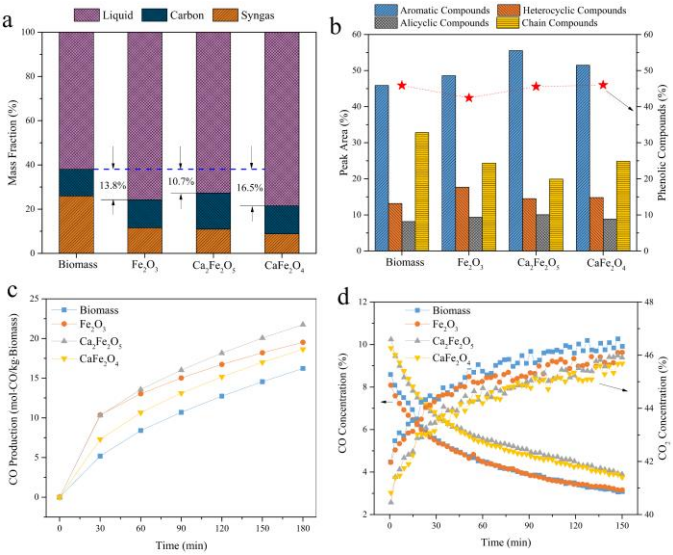

Fig. 5. CO_2 and biomass co-conversion to produce CO with phenolic-rich bio-oil production. a) effect of different Fe-containing materials on products distribution; b) effect of different Fe-containing materials on bio-oil components; c) Cumulative CO production; d) CO concentration and CO_2 concentration.

During CO_2 splitting in the fixed bed reactor, the reduced oxygen carrier, unreacted biochar, and deposited carbon are used for CO_2 splitting. In the first 30 min, CO_2 splitting performance is on the order of $Ca_2Fe_2O_5 \approx Fe_2O_3 > CaFe_2O_4 >$ biomass without OC (Fig. 5c). After 30 min, however, the CO production rate in the presence of Fe_2O_3 decreased gradually with time, whereas it remains a stable CO production rate in the presence of $Ca_2Fe_2O_5$. This is because 1) the $Ca_2Fe_2O_5$ system produced more biochar; 2) the reduced Fe_2O_3 (Fe^0) cannot be completely oxidized by CO_2 to generate its original oxidation state (Fe^{3+}), instead, Fe_3O_4 is produced; and 3) the reduced $Ca_2Fe_2O_5$ (Fe^0) can be fully oxidized by CO_2 to re-from Fe^{3+}. The cumulative CO production with applied Fe_2O_3, $Ca_2Fe_2O_5$, and $CaFe_2O_4$ increased by 20.3%, 28.3%, and 11.1%, respectively, comparing the cumulative CO production without OC addition. Additionally, more CO_2 can be converted to CO by the mixture of reduced $Ca_2Fe_2O_5$/$CaFe_2O_4$ and biochar, resulting in the lower CO_2 concentration and higher CO concentration compared with Fe_2O_3 and without an OC (Fig. 5d). The effect of different $Ca_2Fe_2O_5$ loading on the CO concentration and yields is supplied in Fig. S3.

Results from the fixed bed experiments indicate $Ca_2Fe_2O_5$ is the best performing OC in terms of syngas reduction activity and phenol-rich bio-oil production during biomass cascade utilization as well as CO_2 splitting to CO. For this reason, its cyclic stability was investigated

and compared to that of Fe_2O_3. Results reveal that the $Ca_2Fe_2O_5$ maintains near-perfect activity and cyclic durability even after 50 redox cycles (Fig. 6), and TGA results suggest carbon deposition does not affect the cyclic durability of the $Ca_2Fe_2O_5$ aerogel. It was also observed from the TGA results that carbon deposition decreased and stabilized over multiple cycles. This is because the carbon deposition time is different. For the first several cycles, the complete reduction of $Ca_2Fe_2O_5$ takes fewer time, thus there will be more time for carbon decomposition under the same reduction time; with the number of cycles increases, the OC reduction activity becomes stable, achieving the stable amount of carbon deposition.

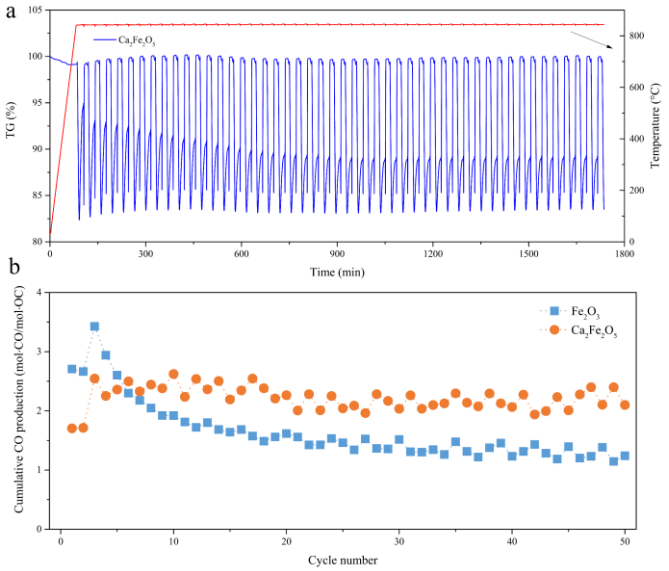

Fig. 6. 50 cycles of chemical looping experiment by using Fe_2O_3 and/or $Ca_2Fe_2O_5$ as the oxygen carriers a) TGA and b) fixed bed experiments.

3.3 Reacted OC characterization

The compositions of the as-prepared, syngas reduced, CO_2 oxidized, and 50th redox cycled a) $Ca_2Fe_2O_5$ and b) $CaFe_2O_4$ were determined by XRD as presented in Fig. 7 (See Fig. S4 for the phase evolution of Fe_2O_3) [60]. Based on XRD results, syngas reduction of the oxygen carriers was as follows: 1) Fe_2O_3 reduction to Fe (JCPDS 87-0721); 2) $Ca_2Fe_2O_5$ reduction to CaO (JCPDS 77-2376), Fe (JCPDS 99-0064), $FeN_{0.056}$ (JCPDS 75-2129), and Fe_3C (JCPDS 72-1110); and 3) $CaFe_2O_4$ reduction to CaO (JCPDS 78-0649), Fe (JCPDS 99-0064), and Fe_3C (JCPDS 85-1317).

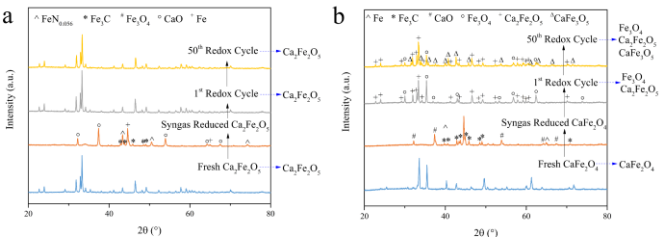

Fig. 7. XRD patterns of fresh, syngas reduced, 1st redox cycled, and 50th redox cycled a) $Ca_2Fe_2O_5$ and b) $CaFe_2O_4$.

To investigate the structural evolution oxygen carriers across many cycles, XRD patterns of the 1st and 50th redox cycles are compared (Fig. 7). In the Fe_2O_3 system, Fe_3O_4 (JCPDS 99-0073) and FeO (JCPDS 75-1550) are the primary phases after 1 cycle and 50 cycles, indicating incomplete oxidation of Fe^0. In the $CaFe_2O_4$ aerogel system, Fe_3O_4 (JCPDS 99-0073) and $Ca_2Fe_2O_5$ (JCPDS 71-2264) are the main components after the first cycle, and $CaFe_3O_5$ (JCPDS 72-0890) appeared in the final cycle, suggesting a portion of the reduced $CaFe_2O_4$ can be completely oxidized by CO_2 and generate to $Ca_2Fe_2O_5$. The other portion of reduced $CaFe_2O_4$ cannot be fully oxidized which produces Fe_3O_4 or $CaFe_3O_5$ ($Fe^{2+, 3+}$). As for the $Ca_2Fe_2O_5$ aerogel system, $Ca_2Fe_2O_5$ (JCPDS 71-2264) remained the dominant species even after 50 redox cycles, demonstrating its superior stability compared to Fe_2O_3 and $CaFe_2O_4$. Thus, considering the efficient utilization rate of the Fe valence and cyclic stability, the three OCs in order of stability are $Ca_2Fe_2O_5$ > $CaFe_2O_4$ > Fe_2O_3.

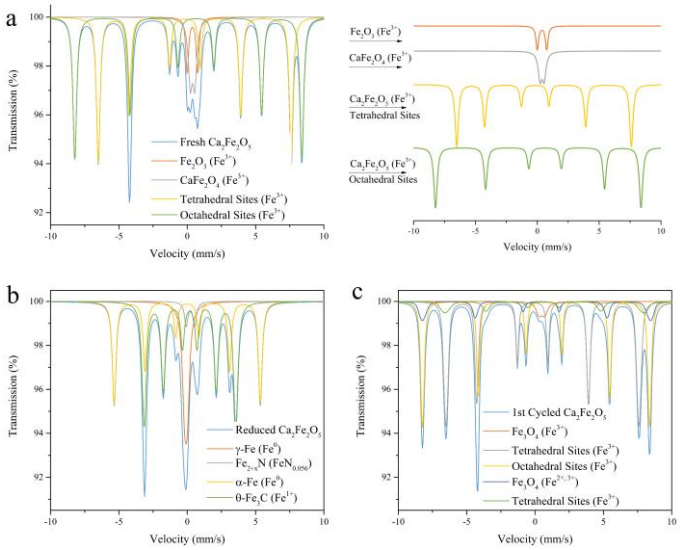

Fig. 8. Mössbauer spectra of a) fresh $Ca_2Fe_2O_5$; b) syngas reduced $Ca_2Fe_2O_5$; and c) $Ca_2Fe_2O_5$ after re-oxidation in the first cycle.

Fe-Mössbauer spectra for fresh $Ca_2Fe_2O_5$, reduced $Ca_2Fe_2O_5$, and 1st redox cycled $Ca_2Fe_2O_5$ were shown in Fig. 8a. The detailed information, isomer shift, quadrupole shift, peak width, internal field, and area (%) can be seen in Table 3. The isomer shift and quadrupole splitting results from the Mössbauer spectra clearly indicate that the Fe species of fresh $Ca_2Fe_2O_5$ aerogel are trivalent [55]. Combined with XRD results, the two doublets were assigned to Fe_2O_3 (site 1, red sub-spectrum) and $CaFe_2O_4$ (site 2, gray sub-spectrum), respectively. Two sextets are allocated to be brownmillerite-type $Ca_2Fe_2O_5$ with two ferric ion sites of tetrahedral (site 3, yellow sub-spectrum) and octahedral (site 4, green sub-spectrum) which accounts for 41% and 42% of the total Mössbauer fit area, indicating $Ca_2Fe_2O_5$ as the dominant phase [20, 61, 62].

For the syngas-reduced $Ca_2Fe_2O_5$, the sextet and singlet components in the Mössbauer spectrum suggest the existence of Fe^0 which are assigned to γ-Fe^0 (site 1) and α-Fe^0 (site 3), accounting for 16% and 33% of the total Mössbauer fit area. The doublet with gray color is attributed to the crystalline structure of ξ-Fe_2N or ε-$Fe_{2+x}N$, which coincides with previous XRD results for $FeN_{0.056}$ (JCPDS 75-2129) [63]. The sextet of green sub-spectrum is assigned to be Fe_3C (site 4, Fe^{1+}) [64]. The redox cycled $Ca_2Fe_2O_5$ spectrum was

ascribed to be 89% trivalent Fe^{3+} (two sextets in tetrahedral site and one sextet in octahedral site) and a small portion Fe (one sextet and one doublet) with Mössbauer parameters consistent with a mixed valent site, denoted by $Fe^{2+,3+}$ (Table 3) [65, 66]. The brownmillerite-type structure ($Ca_2Fe_2O_5$) is relatively stable and was re-oxidized by CO_2 to regenerate Fe^{3+}. For $CaFe_2O_4$ or Fe_2O_3, the reduced Fe^{3+} was not completely re-oxidized by CO_2 under relatively low temperatures (~800 °C), leading to the production of $Fe^{2+,3+}$.

H_2-temperature programmed reduction (H_2-TPR) was performed to compare the reduction activity of Fresh, once cycled, and 50th cycled OCs (Fig. 9). For fresh and once cycled $Ca_2Fe_2O_5$, one main peak was shown in the 400-920 °C temperature range, revealing that the $Ca_2Fe_2O_5$ aerogel is almost pure and was reduced in a single step. The 50th cycled $Ca_2Fe_2O_5$ aerogel peak shifted to slightly higher temperatures (around 30 °C) compared with fresh and 1st cycled $Ca_2Fe_2O_5$, indicating the activity of the OC decreases, which could be caused by the partial sintering and agglomeration of the cycled $Ca_2Fe_2O_5$. The H_2-TPR profiles for $CaFe_2O_4$ and its reduction mechanism vary significantly from that of $Ca_2Fe_2O_5$; namely, one primary peak was shown for the $CaFe_2O_4$, indicating a single reduction by H_2. Results after $CaFe_2O_4$ reduction in the first cycle revealed two main reduction peaks, which are attributed to the reduction of Fe_3O_4 to FeO, and FeO to Fe, respectively. The peaks of the $CaFe_2O_4$ shift to a significantly higher temperature range after 50 redox cycles, owing to the $CaFe_3O_5$ formation (Fig. 7b).

The CO_2-TPO results are provided in Fig. 9b. As can be seen, t the initial oxidation temperature of Fe_2O_3 is approximately 200 °C lower than $Ca_2Fe_2O_5$ and $CaFe_2O_4$ aerogels with a comparatively low oxidation rate. Contrastingly, for $Ca_2Fe_2O_5$ and $CaFe_2O_4$ aerogels, the OC oxidation initiated at temperatures above 400 °C, at which point the rate dramatically increased to rates greater than that of Fe_2O_3. A decrease in mass of the solid is observed for Fe_2O_3, $Ca_2Fe_2O_5$, and $CaFe_2O_4$, which is attributed to carbon oxidation by CO_2. The results are in agreement with the TGA results (Fig. 4a), suggesting that more carbon is deposited with $Ca_2Fe_2O_5$ and $CaFe_2O_4$ as the oxygen carriers. Moreover, the reduced $Ca_2Fe_2O_5$ also has the highest CO_2 splitting activity at temperatures above 800 °C, indicating the CO_2 splitting activity between the oxygen carriers as $Ca_2Fe_2O_5$ > $CaFe_2O_4$ > Fe_2O_3.

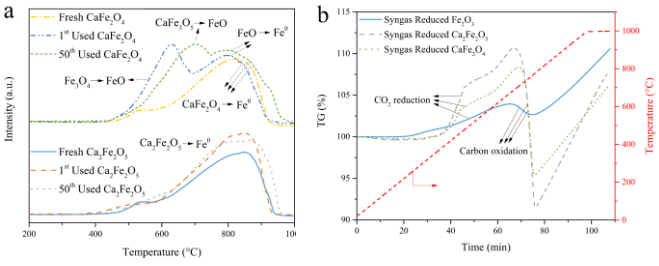

Fig. 9. a) H_2-TPR profiles of Fresh, 1st used, and 50th cycled $Ca_2Fe_2O_5$ and $CaFe_2O_4$ aerogels respectively; b) CO_2-TPO profiles of syngas reduced Fe_2O_3, $Ca_2Fe_2O_5$, and $CaFe_2O_4$.

As can be seen in Fig. 10a and Table 4, the BET surface area of Fe_2O_3 decreased significantly (from 43.6 to 28.9 m^2/g, a 33.7% decrease) between the first and 50th cycles, primarily due to particle sintering and agglomeration of Fe_2O_3. However, the freeze-drying assisted $Ca_2Fe_2O_5$ and $CaFe_2O_4$ were relatively stable; their BET specific surface area decreased by 9.1% and 9.7% (from 65.0 to 59.1 m^2/g, and from 60.9 to 55.0 m^2/g), respectively, between the first and 50th cycle. The pore volume of Fe_2O_3 decreased by 32.7% and 34.3% during the first cycle and between the fresh sample and 50th cycle, compared to 9.0% and 9.8% for $Ca_2Fe_2O_5$ aerogel, and 19.4% and 12.1% for the $CaFe_2O_4$ aerogel (Fig. 10b and Table 4). Thus, the largest single decrease in pore volume occurs during the first redox cycle. It is also observed that the crystallite size of Fe_2O_3 decreases from 75.9 nm to 89.6 nm and 93.7 nm after 1st cycle and 50th cycle, respectively; while for $Ca_2Fe_2O_5$, its crystallite size remains relatively stable even after 50th redox cycles.

Of the tested samples, $Ca_2Fe_2O_5$ and $CaFe_2O_4$ show greater stability to resist the particle sintering and agglomeration. The reasons could be: 1) The freeze-dry assisted nanostructured $Ca_2Fe_2O_5$ and $CaFe_2O_4$ aerogels possess large BET surface areas and pore volumes, showing greater ability for gas diffusion and surface reaction. Thus, the partially sintered and agglomerated aerogels still maintain relatively stable redox activity and cyclic durability; 2) according to the XRD results, a reversible phase transformation ($Ca_2Fe_2O_5$ ↔ Fe + CaO) occurs during syngas reduction and CO_2 oxidation cycles. It is reported by Dang et al. that the phase change ($Ca_3Co_4O_9$ ↔ Co + CaO) suppress the sintering of CaO sorbent and Co catalyst which is ascribed to the homogenized formation of $Ca_3Co_4O_9$ on an atomic level [67]. Similarly, the oxidation of Fe^0 by CO_2 generates $Ca_2Fe_2O_5$ during CO_2 splitting stage which was speculated to suppress the sintering and agglomeration of the cycled OC.

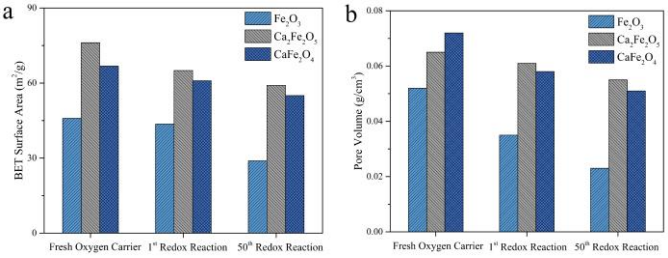

Fig. 10. a) BET surface areas and b) pore volumes of fresh, once-cycled, and 50-cycled aerogels.

SEM images of 1st cycled and 50th cycled $Ca_2Fe_2O_5$ were presented in Fig. 11. It can be concluded that the 1st cycled $Ca_2Fe_2O_5$ aerogel particles are 300-500 nm and the particle size of $Ca_2Fe_2O_5$ are homogenous. $Ca_2Fe_2O_5$ particles after 50th redox cycles exhibited a relatively large particle size due to partial sintering and agglomeration, but still in the micrometre size range. Comparison of the EDS spectra of once-cycled and 50th cycled $Ca_2Fe_2O_5$ samples suggest the existence of Fe, Ca, O, and a small amount of C, which is confirmed by XPS analysis results. Moreover, the comparison of two EDS spectra indicates that the elemental distribution of 1st cycled and 50th cycled samples changed little. The EDS mapping results reveal that the Ca and Fe elements are distributed homogenously for both 1st cycled and 50th cycled $Ca_2Fe_2O_5$ samples for most mapping areas, with slight non-homogeneity in the areas labelled with yellow boxes (Fig. 11b).

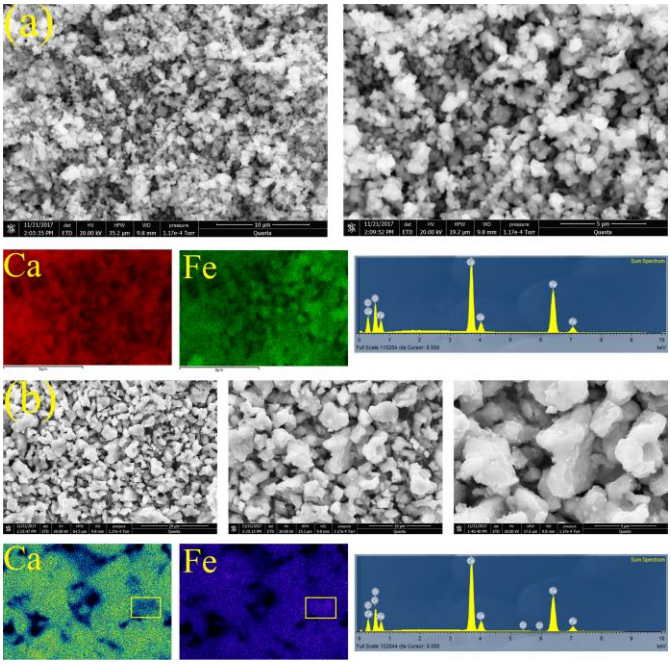

Fig. 11. SEM and EDS mapping results for a) $Ca_2Fe_2O_5$ aerogel after once redox cycle; b) $Ca_2Fe_2O_5$ aerogel after 50 redox cycles.

3.4 Mechanism for synchronous enhancement

Fig. 12 illustrates the proposed mechanism for the simultaneous enhancement of chemical looping CO_2 splitting with biomass cascade utilization using $Ca_2Fe_2O_5$ aerogel as the oxygen carrier. It has been reported that the oxygen carrier plays the roles of generating oxygen ions/vacancies and electrons/holes, facilitating their diffusion in the bulk phase, and providing active sites for surface reactions [68]. In this study, the transformation of lattice oxygen in the reducing environment has been divided into three stages: 1) oxygen species activation at high temperatures; 2) activated oxygen anion permeation from the bulk to the surface of the OC under the oxygen chemical potential gradient; 3) reaction of surface oxygens species with biomass to produce biochar, bio-oil, H_2, CH_4, CO, CO_2, H_2O, and CaO.

The presence of CaO promotes the bio-tar cracking to light components and the existence of intermediates, CO_2 and H_2O, play the role of bio-tar reforming, which synergistically enhance the bio-tar abatement [54, 69, 70]. Moreover, the synchronous enhancement of OC reduction with biomass pyrolysis reflects in: 1) biomass-derived products initially promote the $Ca_2Fe_2O_5$ reduction; 2) the $Ca_2Fe_2O_5$ reduction products, CaO, H_2O, and CO_2, facilitate the bio-tar cracking/reforming with more reducing gas production; 3) the generated reducing gas further accelerates the deep reduction of $Ca_2Fe_2O_5$ to Fe^0. As for CO_2 splitting stage, the presence of Fe^0 and biochar initiates the reduction of CO_2 to CO. The oxygen derived from CO_2 is adsorbed on the OC surface and subsequently diffuses into the bulk OC, and its combination with the oxygen vacancies in the bulk, accomplishing re-oxidation of Fe^0 with formation of $Ca_2Fe_2O_5$ on an atomic level.

4. Conclusions

In this study, $Ca_2Fe_2O_5$ aerogel was prepared using a freeze-dry assisted DIS method using PO and PAA to create a homogeneous and stable, and cost-effective material. The promise of $Ca_2Fe_2O_5$ aerogel as an oxygen carrier was then demonstrated due to its reduction and oxidation activity, phase reversibility, and cyclic stability. A novel chemical looping process was proposed for the synergistic promotion of CO_2 reduction and biomass cascade utilization using $Ca_2Fe_2O_5$ to produce syngas, phenol-rich bio-oil, and high-concentration CO. The mechanism for the synergistic enhancement of chemical looping CO_2 splitting and biomass cascade utilization is also investigated, and it is found the products from biomass fast pyrolysis and OC reduction can further promote OC reduction and biomass conversion, respectively. Similarly, the products from OC reduction and biomass fast pyrolysis synergistically enhance CO_2 reduction.

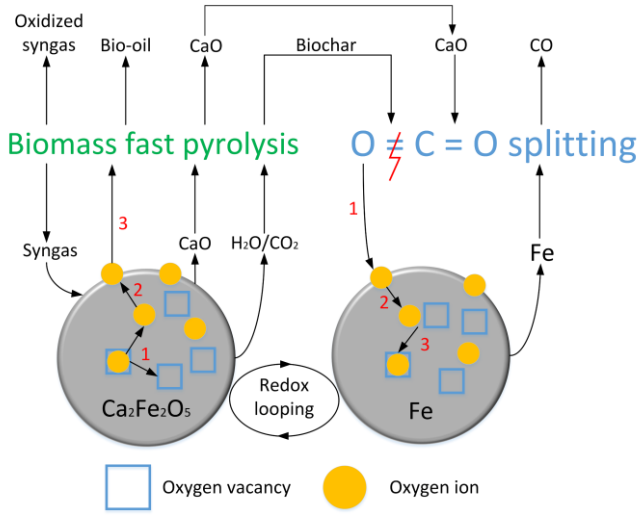

Fig. 12. Schematic of continuous CO_2 to CO conversion and utilization with applied biomass as raw stock and $Ca_2Fe_2O_5$ aerogel as oxygen carrier material.

Acknowledgements

The authors gratefully acknowledge financial support from the National Natural Science Foundation of China (51576042) and National Science Foundation of US (1632899).

Notes and references

1. J. Wang, L. Huang, R. Yang, Z. Zhang, J. Wu, Y. Gao, Q. Wang, D. O'Hare and Z. Zhong, Energy & Environmental Science, 2014, 7, 3478-3518.
2. M. Mikkelsen, M. Jørgensen and F. C. Krebs, Energy & Environmental Science, 2010, 3, 43-81.
3. S. Choi, J. H. Drese and C. W. Jones, ChemSusChem, 2009, 2, 796-854.
4. M. Bui, C. S. Adjiman, A. Bardow, E. J. Anthony, A. Boston, S. Brown, P. S. Fennell, S. Fuss, A. Galindo and L. A. Hackett, Energy & Environmental Science, 2018.
5. M. S. Duyar, M. A. A. Treviño and R. J. Farrauto, Applied Catalysis B: Environmental, 2015, 168, 370-376.

6. V. M. Lebarbier, R. A. Dagle, L. Kovarik, K. O. Albrecht, X. Li, L. Li, C. E. Taylor, X. Bao and Y. Wang, Applied Catalysis B: Environmental, 2014, 144, 223-232.
7. M. Aresta and A. Dibenedetto, Dalton Transactions, 2007, 2975-2992.
8. M. E. Boot-Handford, J. C. Abanades, E. J. Anthony, M. J. Blunt, S. Brandani, N. Mac Dowell, J. R. Fernández, M.-C. Ferrari, R. Gross and J. P. Hallett, Energy & Environmental Science, 2014, 7, 130-189.
9. L. C. Buelens, V. V. Galvita, H. Poelman, C. Detavernier and G. B. Marin, science, 2016, 354, 449-452.
10. G. Centi, E. A. Quadrelli and S. Perathoner, Energy & Environmental Science, 2013, 6, 1711-1731.
11. L. Li, N. Zhao, W. Wei and Y. Sun, Fuel, 2013, 108, 112-130.
12. Y. Du, H. Yang, S. Wan, Y. Jin and W. Zhang, Journal of Materials Chemistry A, 2017, 5, 9163-9168.
13. M. H. Kim, T. Song, U. R. Seo, J. E. Park, K. Cho, S. M. Lee, H. J. Kim, Y.-J. Ko, Y. K. Chung and S. U. Son, Journal of Materials Chemistry A, 2017, 5, 23612-23619.
14. W. C. Chueh, C. Falter, M. Abbott, D. Scipio, P. Furler, S. M. Haile and A. Steinfeld, Science, 2010, 330, 1797-1801.
15. A. H. McDaniel, E. C. Miller, D. Arifin, A. Ambrosini, E. N. Coker, R. O'Hayre, W. C. Chueh and J. Tong, Energy & Environmental Science, 2013, 6, 2424-2428.
16. J. R. Scheffe and A. Steinfeld, Materials Today, 2014, 17, 341-348.
17. D. Yap, J.-M. Tatibouët and C. Batiot-Dupeyrat, Journal of CO2 Utilization, 2015, 12, 54-61.
18. D. S. Mallapragada, N. R. Singh, V. Curteanu and R. Agrawal, Industrial & Engineering Chemistry Research, 2013, 52, 5136-5144.
19. N. A. Dharanipragada, L. C. Buelens, H. Poelman, E. De Grave, V. V. Galvita and G. B. Marin, Journal of Materials Chemistry A, 2015, 3, 16251-16262.
20. Z. Sun, S. Chen, J. Hu, A. Chen, A. H. Rony, C. K. Russell, W. Xiang, M. Fan, M. D. Dyar and E. C. Dklute, Applied Energy, 2018, 211, 431-442.
21. K. Li, X. Cheng, N. Li, X. Zhu, Y. Wei, K. Zhai and H. Wang, Journal of Materials Chemistry A, 2017, 5, 24232-24246.
22. G. Deng, K. Li, Z. Gu, X. Zhu, Y. Wei, X. Cheng and H. Wang, Chemical Engineering Journal, 2018, 341, 588-600.
23. V. V. Galvita, H. Poelman, C. Detavernier and G. B. Marin, Applied Catalysis B: Environmental, 2015, 164, 184-191.
24. J. Hu, L. Buelens, S.-A. Theofanidis, V. V. Galvita, H. Poelman and G. B. Marin, Journal of CO_2 Utilization, 2016, 16, 8-16.
25. J. Hu, V. V. Galvita, H. Poelman, C. Detavernier and G. B. Marin, Applied Catalysis B: Environmental, 2018, 231, 123-136.
26. C. Lu, K. Li, H. Wang, X. Zhu, Y. Wei, M. Zheng and C. Zeng, Applied Energy, 2018, 211, 1-14.
27. Y. Zheng, K. Li, H. Wang, D. Tian, Y. Wang, X. Zhu, Y. Wei, M. Zheng and Y. Luo, Applied Catalysis B: Environmental, 2017, 202, 51-63.
28. Y. A. Daza, R. A. Kent, M. M. Yung and J. N. Kuhn, Industrial & Engineering Chemistry Research, 2014, 53, 5828-5837.
29. Y. A. Daza, D. Maiti, R. A. Kent, V. R. Bhethanabotla and J. N. Kuhn, Catalysis Today, 2015, 258, 691-698.
30. A. Abad, J. Adánez, F. García-Labiano, F. Luis, P. Gayán and J. Celaya, Chemical Engineering Science, 2007, 62, 533-549.
31. P. Cho, T. Mattisson and A. Lyngfelt, Fuel, 2004, 83, 1215-1225.
32. V. V. Galvita, M. Filez, H. Poelman, V. Bliznuk and G. B. Marin, Catalysis letters, 2014, 144, 32-43.
33. N. L. Galinsky, A. Shafiefarhood, Y. Chen, L. Neal and F. Li, Applied Catalysis B: Environmental, 2015, 164, 371-379.
34. M. Tang, L. Xu and M. Fan, Applied Energy, 2015, 151, 143-156.
35. V. V. Galvita, H. Poelman and G. B. Marin, Topics in Catalysis, 2011, 54, 907.
36. J. Adanez, A. Abad, F. Garcia-Labiano, P. Gayan and F. Luis, Progress in Energy and Combustion Science, 2012, 38, 215-282.
37. T. Mattisson, A. Järdnäs and A. Lyngfelt, Energy & Fuels, 2003, 17, 643-651.
38. Q. Zafar, T. Mattisson and B. Gevert, Energy & Fuels, 2006, 20, 34-44.
39. D. D. Miller and R. Siriwardane, Energy & Fuels, 2013, 27, 4087-4096.
40. C. D. Bohn, C. R. Müller, J. P. Cleeton, A. N. Hayhurst, J. F. Davidson, S. A. Scott and J. S. Dennis, Industrial & Engineering Chemistry Research, 2008, 47, 7623-7630.
41. S. Wang, G. Wang, F. Jiang, M. Luo and H. Li, Energy & Environmental Science, 2010, 3, 1353.
42. M. S. Chan, W. Liu, M. Ismail, Y. Yang, S. A. Scott and J. S. Dennis, Chemical Engineering Journal, 2016, 296, 406-411.
43. I. Zamboni, C. Courson and A. Kiennemann, Applied Catalysis B: Environmental, 2017, 203, 154-165.
44. X. Wu, G. Shao, X. Shen, S. Cui and X. Chen, Chemical Engineering Journal, 2017, 330, 1022-1034.
45. X. Jia, B. Dai, Z. Zhu, J. Wang, W. Qiao, D. Long and L. Ling, Carbon, 2016, 108, 551-560.
46. Q. Lei, H. Song, X. Chen, M. Li, A. Li, B. Tang and D. Zhou, RSC Advances, 2016, 6, 40683-40690.
47. H. Ren, L. Zhang, C. Shang, X. Wang and Y. Bi, Journal of sol-gel science and technology, 2010, 53, 307-311.
48. Y. Tokudome, A. Miyasaka, K. Nakanishi and T. Hanada, Journal of sol-gel science and technology, 2011, 57, 269-278.
49. A. E. Gash, J. H. Satcher and R. L. Simpson, Journal of Non-Crystalline Solids, 2004, 350, 145-151.
50. C. N. Sisk and L. J. Hope-Weeks, Journal of Materials Chemistry, 2008, 18, 2607-2610.
51. Y. P. Gao, C. N. Sisk and L. J. Hope-Weeks, Chemistry of Materials, 2007, 19, 6007-6011.
52. A. Du, B. Zhou, J. Shen, S. Xiao, Z. Zhang, C. Liu and M. Zhang, Journal of Non-Crystalline Solids, 2009, 355, 175-181.
53. Y. Bi, H. Ren, B. Chen, G. Chen, Y. Mei and L. Zhang, Journal of sol-gel science and technology, 2012, 63, 140-145.
54. Z. Sun, S. Chen, C. K. Russell, J. Hu, A. H. Rony, G. Tan, A. Chen, L. Duan, J. Boman and J. Tang, Applied Energy, 2018, 212, 931-943.
55. M. D. Dyar, D. G. Agresti, M. W. Schaefer, C. A. Grant and E. C. Sklute, Annu. Rev. Earth Planet. Sci., 2006, 34, 83-125.
56. Z. Sun, B. Xu, A. H. Rony, S. Toan, S. Chen, K. A. Gasem, H. Adidharma, M. Fan and W. Xiang, Energy Conversion and Management, 2017, 146, 182-194.
57. A. Veses, M. Aznar, I. Martínez, J. D. Martínez, J. M. López, M. V. Navarro, M. S. Callén, R. Murillo and T. García, Bioresource Technology, 2014, 162, 250-258.
58. S. Liu, Q. Xie, B. Zhang, Y. Cheng, Y. Liu, P. Chen and R. Ruan, Bioresource Technology, 2016, 204, 164-170.

59. Z. Sun, B. Xu, A. H. Rony, S. Toan, S. Chen, K. A. M. Gasem, H. Adidharma, M. Fan and W. Xiang, Energy Conversion and Management, 2017, 146, 182-194.
60. B.-j. Xue, J. Luo, F. Zhang and Z. Fang, Energy, 2014, 68, 584-591.
61. D. Hirabayashi, Y. Sakai, T. Yoshikawa, K. Mochizuki, Y. Kojima, K. Suzuki, K. Ohshita and Y. Watanabe, Hyperfine interactions, 2006, 167, 809-813.
62. I. Zamboni, C. Courson and A. Kiennemann, Applied Catalysis B: Environmental, 2017, 203, 154-165.
63. A. Zitolo, V. Goellner, V. Armel, M.-T. Sougrati, T. Mineva, L. Stievano, E. Fonda and F. Jaouen, Nature materials, 2015, 14, 937.
64. X.-W. Liu, S. Zhao, Y. Meng, Q. Peng, A. K. Dearden, C.-F. Huo, Y. Yang, Y.-W. Li and X.-D. Wen, Scientific reports, 2016, 6, 26184.
65. P. B. Rathod, A. K. Pandey, S. S. Meena and A. A. Athawale, RSC Advances, 2016, 6, 21317-21325.
66. L. H. Singh, S. S. Pati, M. J. Sales, E. M. Guimarães, A. C. Oliveira and V. K. Garg, Journal of the Brazilian Chemical Society, 2015, 26, 2214-2223.
67. C. Dang, Y. Li, S. M. Yusuf, Y. Cao, H. Wang, H. Yu, F. Peng and F. Li, Energy & Environmental Science, 2018, 11, 660-668.
68. L. Zeng, Z. Cheng, J. A. Fan, L.-S. Fan and J. Gong, Nature Reviews Chemistry, 2018, 1.
69. B. Zhang, L. Zhang, Z. Yang, Y. Yan, G. Pu and M. Guo, International Journal of Hydrogen Energy, 2015, 40, 8816-8823.
70. Z. Sun, S. Toan, S. Chen, W. Xiang, M. Fan, M. Zhu and S. Ma, International Journal of Hydrogen Energy, 2017, 42, 16031-16044.

Table 1 Proximate and ultimate analysis of the pine wood.

Proximate analysis (% by weight)	
Fixed carbon	16.50
Volatile	78.12
Moisture	5.09
Ash	0.29
Ultimate analysis (% by weight)	
Carbon	50.36
Hydrogen	6.20
Nitrogen	0.33
Oxygen	43.06
Sulfur	0.05

Table 2 Ash composition of pine wood samples by using XRF analysis.

Compound	Biomass ash (%)
SiO_2	6.45
Al_2O_3	1.93
Fe_2O_3	2.54
CaO	42.90
MgO	13.61
Na_2O	1.05
K_2O	14.76
MnO_2	3.58
P_2O_5	2.69
SrO	0.24
BaO	0.18
SO_3	1.63

Table 3 Mossbauer results of Fresh $Ca_2Fe_2O_5$, syngas reduced $Ca_2Fe_2O_5$, and 1st redox cycled $Ca_2Fe_2O_5$.

	Fresh $Ca_2Fe_2O_5$			
	Site 1 Fe^{3+}	Site 2 Fe^{3+}	Site 3 Fe^{3+} (tetrahedral)	Site 4 Fe^{3+} (octahedral)
Isomer Shift (mm/s)	0.38	0.39	0.19*	0.35
Quadrupole Shift (mm/s)	0.77	0.33	0.72*	-0.55
Peak Width (mm/s)	0.24*	0.35	0.29*	0.3
Internal Field (kOe)	N/A	N/A	438	515.2
Area (%)	6	10	41	42
Normalized Chi Squared	13.3			
	Syngas reduced $Ca_2Fe_2O_5$			
	Site 1 Fe^{0}	Site 2 $Fe^{0.17}$	Site 3 Fe^{0}	Site 4 Fe^{+1}
Isomer Shift (mm/s)	-0.07	0.23	0	0.19
Quadrupole Shift (mm/s)	0.0*	0.71	0	0.02
Peak Width (mm/s)	0.37	0.30*	0.3	0.33
Internal Field (kOe)	N/A	N/A	332	206.5
Area (%)	16	4	33	46
Normalized Chi Squared	6			
	1st cycled $Ca_2Fe_2O_5$				
	Site 1 $Fe^{2+, 3+}$	Site 2 Fe^{3+} (tetrahedral)	Site 3 Fe^{3+} (octahedral)	Site 4 Fe^{3+} (octahedral)	Site 5 $Fe^{2+, 3+}$
Isomer Shift (mm/s)	0.5	0.183	0.36	0.28	0.65
Quadrupole Shift (mm/s)	0.42	0.721	-0.6	-0.34	0.06
Peak Width (mm/s)	0.50*	0.22*	0.22*	0.30*	0.40*
Internal Field (kOe)	N/A	437.8	515	518.4	453
Area (%)	3	43	36	10	9
Normalized Chi Squared	18				

* indicates fixed parameter. Note that the chi squared values are high due to high signal to noise.

Table 4 Physical properties of as-prepared, reacted, and cycled Fe_2O_3, $Ca_2Fe_2O_5$, and $CaFe_2O_4$.

Catalyst	Crystallite Size [a] (nm)	Average pore Diameter (nm)	BET surface area (m^2/g)	Pore volume (g/cm^3)
Fresh Fe_2O_3	75.9	5.2	45.9	0.052
Fresh $Ca_2Fe_2O_5$	43.6	4.0	76.1	0.067
Fresh $CaFe_2O_4$	39.1	4.5	66.8	0.072
Reduced Fe_2O_3	61.1	3.7	61.2	0.054
Reduced $Ca_2Fe_2O_5$	64.3	4.1	70.8	0.069
Reduced $CaFe_2O_4$	70.8	4.5	66.9	0.075
1^{st} reacted Fe_2O_3	89.6	3.6	43.6	0.035
1^{st} reacted $Ca_2Fe_2O_5$	47.7	3.9	65.0	0.061
1^{st} reacted $CaFe_2O_4$	41.0	4.0	60.9	0.058
50^{th} reacted Fe_2O_3	93.7	3.7	28.9	0.023
50^{th} reacted $Ca_2Fe_2O_5$	41.0	3.9	59.1	0.055
50^{th} reacted $CaFe_2O_4$	37.3	3.8	55.0	0.051

[a] Determined by the Scherrer's equation from the main crystal peaks in XRD patterns.

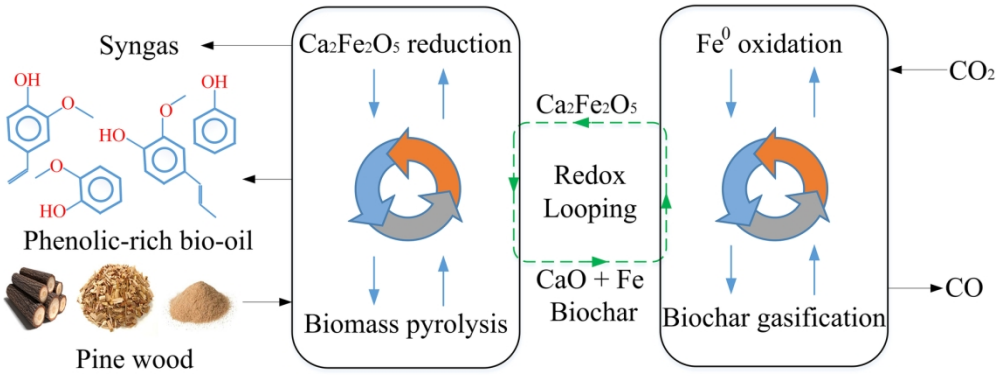

For table of content entry.
A novel chemical looping process to achieve synergistic enhancement of biomass cascade utilization and CO2 splitting

79x30mm (600 x 600 DPI)